

Article

The Preparation of Ti–Ta Impedance-Graded Coatings with Limited Diffusion by Cold Spraying Combined with Hot Isostatic Pressing

Yaoning Shen ¹, Xianjin Ning ^{1,*}, Xiaodong Yu ¹, Dongwei Li ², Chengliang Feng ² and Chengwen Tan ^{1,*}¹ School of Materials Science and Engineering, Beijing Institute of Technology, Beijing 100081, China² Chongqing Hongyu Precision Industry Group Co., Ltd., Chongqing 400000, China

* Correspondence: nxj@bit.edu.cn (X.N.); tanchengwen@bit.edu.cn (C.T.)

Abstract: Ti–Ta impedance-graded coatings were prepared using cold spraying combined with hot isostatic pressing. Compared to the general Ti–Ta binary diffusion couple, the interdiffusion coefficient of as-sprayed Ti–Ta can be increased by approximately 25 times at 1100 °C due to grain refinement at the interface of the cold-sprayed particles. By the control of interdiffusion, pure Ta and pure Ti regions can remain in the materials after hot isostatic pressing at 900 °C. Hot isostatic pressing with capsule reduced the porosity of the material efficiently to less than 0.02%. The strength of the as-sprayed Ti–Ta composite coating was significantly improved to 990.1 MPa, and the fracture strain reached 11.5%. The strengthening mechanism of Ti–Ta composite coatings relies primarily on the hindrance of dislocation slip by phase interfaces between α and β . Moreover, the macroscopic interfacial bonding strength of the graded material exceeds 881 MPa, which is comparable to that of bulk materials.

Keywords: cold spraying; hot isostatic pressing; impedance-graded coatings; mechanical property



Citation: Shen, Y.; Ning, X.; Yu, X.; Li, D.; Feng, C.; Tan, C. The Preparation of Ti–Ta Impedance-Graded Coatings with Limited Diffusion by Cold Spraying Combined with Hot Isostatic Pressing. *Coatings* **2024**, *14*, 565. <https://doi.org/10.3390/coatings14050565>

Academic Editor: Vincent Ji

Received: 14 March 2024

Revised: 19 April 2024

Accepted: 30 April 2024

Published: 2 May 2024



Copyright: © 2024 by the authors. Licensee MDPI, Basel, Switzerland. This article is an open access article distributed under the terms and conditions of the Creative Commons Attribution (CC BY) license (<https://creativecommons.org/licenses/by/4.0/>).

1. Introduction

The impedance-graded materials (IGMs) formed by the stacking of different homogeneous layers can attenuate stress waves effectively and have good potential for application in lightweight protective structures [1–3]. In such IGMs, the stress waves can be attenuated by the transmission and reflection at the macroscopic interfaces as well as by the energy absorption by the plastic deformation of each layer [2,4,5]. When the layer of IGMs consists of particle composite, the spreading, scattering, and dissipating by the complex microscopic interface can further attenuate the stress wave [6,7]. Due to the large difference in the densities of Ti and Ta, the impedance can be flexibly adjusted over a relatively large range for the Ti–Ta composite layer. Meanwhile, the good plasticity of Ti and Ta is beneficial for the tensile plasticity of the Ti–Ta composite, which can resist the tensile stress generated by impedance mismatch at the interface of Ti–Ta IGMs.

Although laser additive manufacturing (LAM) is an attractive method to achieve the specific-shape graded structure, the high temperature involved in LAM may lead to the overreaction of components, phase transformation, and severe thermal stress [8,9]. As a low-temperature solid-state deposition technique, cold spraying (CS) can regulate the composition of each layer flexibly and avoid the phase transformation and reactions during deposition [10,11]. Nevertheless, the tensile strength and plasticity of the as-sprayed coating is often insufficient due to the severe plastic deformation of the particles and the physical-type interfacial bonding between particles [12–15]. Therefore, subsequent heat treatment is often necessary to improve the tensile performance of the cold-sprayed coating by the interfacial diffusion of particles [14,16,17].

For the post-annealing of the Ti–Ta composite coatings, the diffusion occurs at the Ti/Ta interface as well as at Ti/Ti and Ta/Ta interfaces. Although the interdiffusion

at the Ti/Ta interface can promote the bonding property, excessive diffusion arises at too-high temperatures and may lead to the formation of Kirkendall pores, which are detrimental to the mechanical properties of the Ti–Ta coating. Xu et al. [18] proved that the Kirkendall effect increased the porosity significantly during spark plasma sintering (SPS) of Ti–Ta composite powder at 1400 °C. Furthermore, Tang et al. [19] indicated that the large Kirkendall pores reduced the tensile strength of cold-sprayed Ti–Ta coatings significantly after the annealing of 2 h at 1250 °C. Therefore, the adequate treatment temperature is desirable to activate the effective diffusion and, at the same time, to avoid excessive alloying. Up to now, most investigations of Ti–Ta interdiffusion behavior have focused on temperatures much higher than the phase transition temperature of Ti [20–22]. Moreover, the high-speed impact of particles during cold spraying can result in a large number of broken grains near the particle interface and increase the grain boundaries significantly [23,24], which might influence the diffusion process. Unfortunately, few data can be found for the influence of such microstructural characteristics on the diffusion behavior of cold-sprayed Ti–Ta coatings.

Another goal of the post-heat treatment is the elimination of the pores in cold-sprayed coatings. It has been proved that HIP is an effective method to eliminate most of the closed pores in LAMed materials [25,26]. However, the weak physical bonding between particles in cold-sprayed materials may affect the elimination process of pores during HIP. It was found that the elimination of pores in cold-sprayed coatings results in quite different densification characteristics from those of the LAMed materials [27–32]. Due to the dramatically different melting points of Ti and Ta (1670 °C and 3020 °C) [19] and the involvement of Ti/Ta interfacial interdiffusion, the situation of densification becomes more complex.

In this study, cold-spraying accompanied with HIP was used to prepare Ti–Ta impedance-graded coatings. The diffusion behavior of the cold-sprayed Ti–Ta couple was analyzed systematically, and a reasonable diffusion temperature for the Ti–Ta coating was obtained. The influence of unencapsulated and encapsulated HIP on the microstructure and mechanical properties of cold-sprayed Ti–Ta graded coatings was investigated. The strengthening mechanism of the Ti–Ta coating and the possible densification process of the pores during HIP were also discussed.

2. Materials and Experimental Procedures

2.1. Preparation of Ti–Ta Couples and Ti–Ta Graded Coating

Figure 1 presents the size distribution and morphology of the spherical Ti and Ta powders. The size distribution measured by laser particle-size analyzer (Hydro 2000 MU, Malvern Panalytical, Malvern, UK) shows that the average sizes (D_{50}) of Ti and Ta powders are 37.2 μm and 6.7 μm , respectively. The high-pressure cold-spraying system (PCS-100, Plasma Giken Co., Ltd., Saitama, Japan) was used to deposit coatings. The working gas for cold spraying was N_2 with a pressure and temperature of 5.0 MPa and 850–900 °C, respectively. The lateral speed of the spray gun was 400 mm/s, and the spraying distance was fixed at 30 mm.

The Ti–Ta diffusion couples were prepared by depositing a Ta coating with a thickness of about 300 μm on a pre-polished pure Ti plate of 2.5 mm thick. Then, the as-deposited Ti–Ta diffusion couples were sealed in a quartz tube filled with 2×10^5 Pa of argon gas for the post-diffusion annealing.

As for Ti–Ta graded coating, the feedstock powder of cold spraying was obtained by mechanically mixing Ti and Ta powders with mass ratios of 1:1.5, 1:1, and 1:0.6, respectively. Then, the Ti–Ta composite coatings with a width of $50 \times 50 \text{ mm}^2$ were deposited on the Al substrate with a size of $60 \times 50 \times 20 \text{ mm}^3$. Before depositing the next layer, the thickness of the previously deposited coating was processed to about 15 mm. The single layer was labeled according to the mass ratio of the feedstock powder. Figure 2a shows the schematic diagram of the prepared Ti–Ta graded coating, with the coatings labeled as T–Ta_{1.5}, Ti–Ta_{1.0}, and Ti–Ta_{0.6} from bottom to top. After spraying, the substrate was

removed, and the composite coating was cut into samples using wire cutting for the subsequent treatment. The size of tensile sample is shown in Figure 2b.

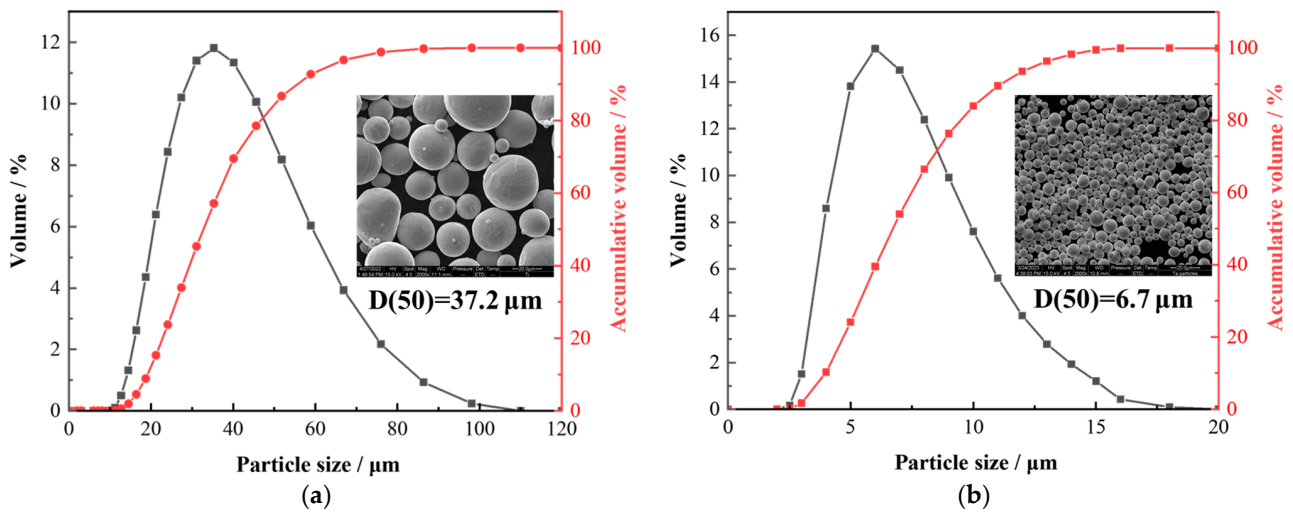


Figure 1. Characterization of original powders: (a) Ti; (b) Ta.

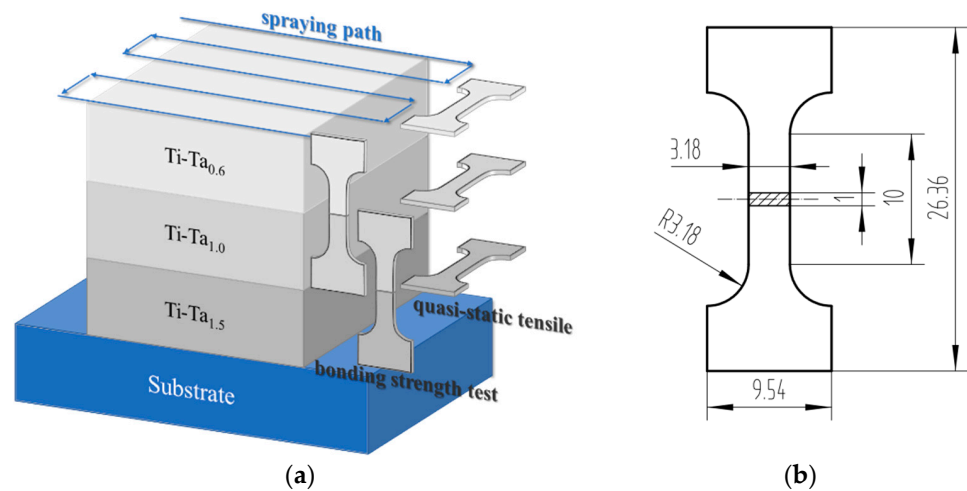


Figure 2. Schematic diagram of (a) cold-sprayed Ti-Ta graded coating and cutting position of samples; (b) size of the tensile samples.

2.2. Interdiffusion Behavior of Ti-Ta Couples

The cold-sprayed Ti-Ta diffusion couples were annealed at 850~1150 °C for 2 h. Figure 3 is a schematic concentration distribution curve of Ta in the Ti-Ta binary diffusion couple. The interdiffusion coefficient (\tilde{D}) between Ti and Ta can be calculated by the Boltzmann–Matano method [33]:

$$\tilde{D} = -\frac{1}{2t} \frac{\int_{C_L}^{C^*} (x - x_M) dC}{\left(\frac{dC}{dx}\right)_{C^*}}, \tag{1}$$

where t is the diffusion time, and C_L and C_R are the Ta concentration on the left and right sides of the initial interface at $t = 0$, respectively. The x_M is the position of the Matano plane. According to the mass conservation, the integral areas on both sides of the Matano plane are equal, which means the area of the yellow and green regions in Figure 3 are equal; then, x_M can be calculated. $(dC/dx)_{C^*}$ is the slope at an arbitrary concentration C^* on the concentration distribution curve, and $\int_{C_L}^{C^*} x dC$ is the integral area (A^*).

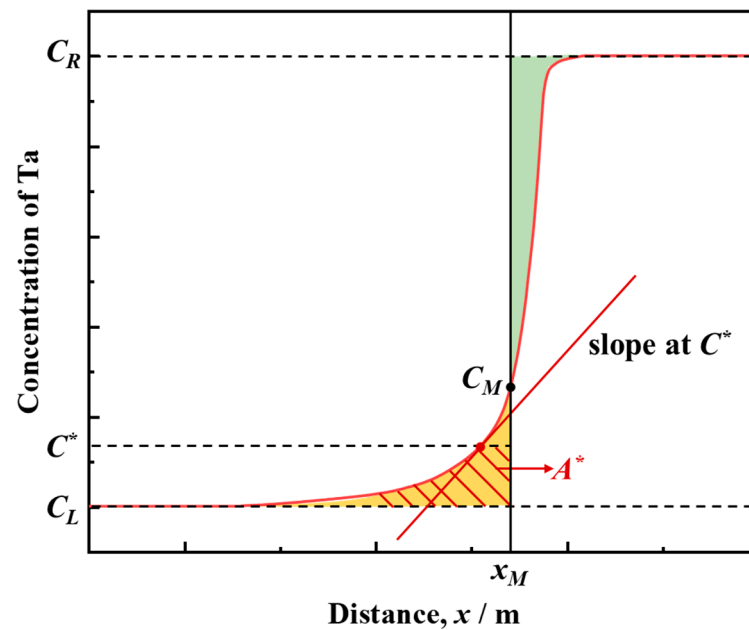


Figure 3. Schematic diagram of the Boltzmann–Matano method for the Ti–Ta diffusion couple.

2.3. HIP Treatment and the Characterization

The cold-sprayed Ti–Ta graded coatings were subjected to 2 h of unencapsulated and encapsulated HIP at a typical temperature of 900 °C. In the latter case, the sample was enclosed in a 2 mm thick 304 stainless steel capsule and vacuumed to 2×10^{-3} Pa before HIP. Ar was used as a protective gas in the HIP furnace with a gas pressure of 140 MPa.

The mechanical properties of each layer of material and the bonding strength of the macroscopic interface in the graded coatings were evaluated through quasi-static tensile test. The cutting position of sample is shown in Figure 2 schematically. The Instron universal testing machine was used for quasi-static tensile tests, with a strain rate of $\sim 10^{-3} \cdot \text{s}^{-1}$. For each case, at least three tests were performed to ensure the reproducibility of the results.

The microstructure of the prepared graded material was analyzed by field emission scanning electron microscopy (SEM, FEI QUANTA 200 FEG, FEI, Hillsboro, OR, USA) equipped with an energy dispersive spectrometer (EDS). The pores in Ti–Ta coatings were analyzed by optical microscopy (OM, OLYMPUS BX51M, Olympus Corporation, Tokyo, Japan), and the porosity was statistically analyzed using ImageJ 1.8.0 software (National Institutes of Health, Bethesda, MD, USA). An electron backscatter diffraction instrument (EBSD, JSM-7900F, JEOL, Tokyo, Japan) was used to observe the recrystallization of Ta particles in Ti–Ta diffusion couple. During the EBSD process, the sample tilt angle was 70° and the scanning step length was 100 nm.

3. Results and Discussion

3.1. Interdiffusion Behavior of Cold-Sprayed Ti–Ta

From the concentration distribution in the Ti–Ta diffusion couple, the diffusion thickness on the Ta (δ_{Ta}) and Ti (δ_{Ti}) sides relative to the initial interface can be calculated. Figure 4 summarizes the diffusion thickness in each diffusion couple after diffusion at 850 °C~1150 °C for 2 h. It is clear that all the diffusion thickness on the Ti side is greater than that on the Ta side, and the growth rate of δ_{Ti} with the increase of temperature is higher than that of δ_{Ta} .

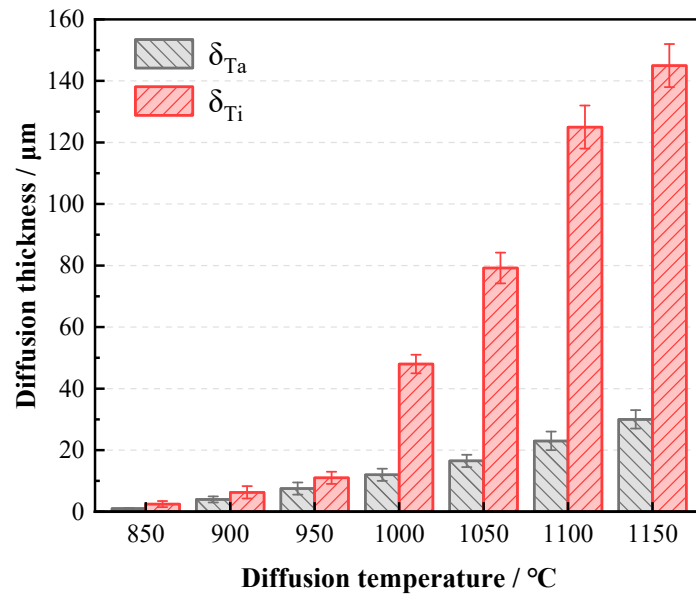


Figure 4. Thickness of diffusion layer in Ti–Ta diffusion couple at different diffusion temperatures.

Figure 5 plots the concentration dependence of the calculated interdiffusion coefficient \tilde{D} of the cold-sprayed Ti–Ta couple under different temperatures. At the range of 850 $^{\circ}\text{C}$ to 950 $^{\circ}\text{C}$, the concentration dependence of \tilde{D} is relatively weak (Figure 5a), which is corresponding to the similar diffusion thicknesses on the Ta and Ti sides (Figure 4). It is worth noting that the interdiffusion coefficient increased significantly by about 10 times as the diffusion temperature increased from 850 $^{\circ}\text{C}$ to 900 $^{\circ}\text{C}$. Since the α (hcp) \rightarrow β (bcc) phase transition of Ti can occur at around 882 $^{\circ}\text{C}$ [34], the bcc structure at 900 $^{\circ}\text{C}$ can lead to lower diffusion activation energy for the Ti atoms. At the same time, a large number of vacancies resulting from phase transformations from the hcp to bcc structure can also promote the interdiffusion [35,36]. Therefore, it is suggested that this abrupt change in the interdiffusion coefficient between 850 $^{\circ}\text{C}$ and 900 $^{\circ}\text{C}$ could be attributed to the phase transition of Ti.

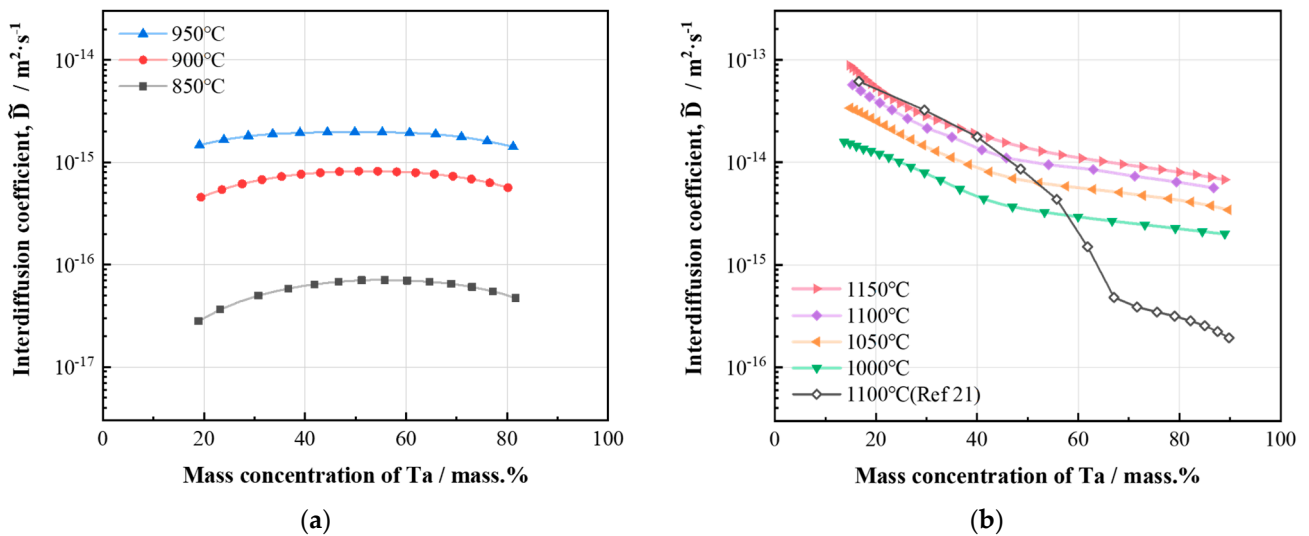


Figure 5. The \tilde{D} of Ti–Ta at different diffusion temperatures: (a) 850–950 $^{\circ}\text{C}$, (b) 1000–1150 $^{\circ}\text{C}$.

At the diffusion temperature range of 1000 $^{\circ}\text{C}$ to 1150 $^{\circ}\text{C}$, the interdiffusion coefficient decreases monotonously with the increase in the Ta concentration (Figure 5b). Similar behavior has been observed by Ansel et al. [21] and Wang et al. [22]. As a comparison,

the \tilde{D} of Ti–Ta calculated by Ansel et al. [21] at 1100 °C is also provided in Figure 5b. It is obvious that the Ansel's curve deviates gradually as the concentration of Ta exceeds 50 wt.%. For instance, the interdiffusion coefficient measured for 85 wt.% Ta in this study is about 25 times that of Ansel's one.

It has been widely accepted that many broken crystals are generated in cold-sprayed coatings due to the violent impact and severe plastic deformation of particles [24,37,38]. During post-heat treatment, e.g., HIP, such broken crystals may experience recrystallization and size growing. Figure 6 shows the EBSD morphology of Ta crystals in the as-sprayed and diffused couple. A large number of extremely fine crystals can be observed at the particle interface in the as-sprayed Ta coating that arose from the severe shear deformation of Ta particles (Figure 6a). After the diffusion at 900 °C, the recrystallization of the fine crystals can be observed preferentially (Figure 6b). At 1000 °C, the flat-shaped grains at the particle's center begin to recrystallize and form the equiaxed grains with small sizes (Figure 6c). When the diffusion temperature increases to 1100 °C, all the grains exhibit equiaxed crystals, and the average grain size is comparable to the size of feedstock Ta powder. Considering the dependence of the growth of grains on diffusion time, the Ti–Ta couple was also diffused at 900 °C for 0.5 h, and the results are shown in Figure 7. It can be found that there is still a large number of small broken crystals in such case, and the average grain size is much smaller than that for 2 h (Figure 6b). Therefore, it can be inferred that at a diffusion temperature of 1100 °C, even the recrystallization and growth rate is much higher; an initial stage must exist during which the grains might be relatively small. Since the grain boundary is the important channel of diffusion [39], it can be supposed that the grain boundary at the initial stage plays a major role in the higher value of \tilde{D} in the Ta-rich region than Ansel's value.

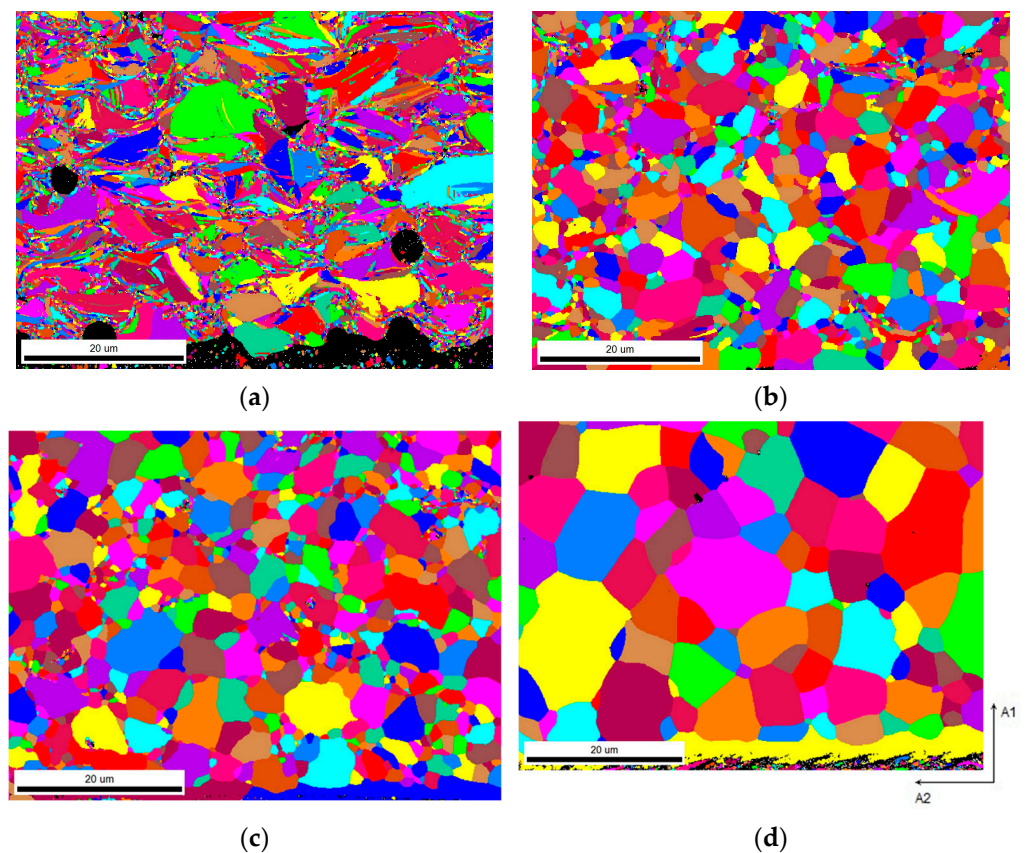


Figure 6. EBSD grain morphology in Ta coating cold-sprayed and diffused at different temperatures for 2 h: (a) as-sprayed; (b) 900 °C; (c) 1000 °C; (d) 1100 °C.

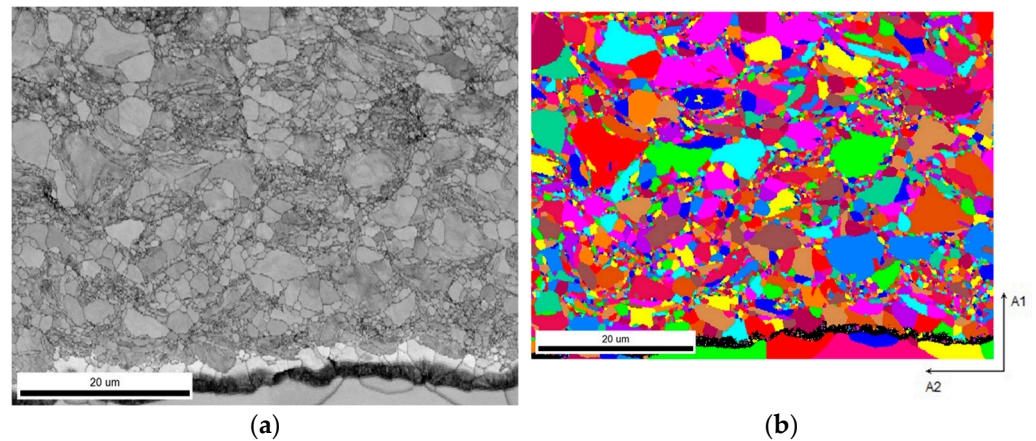


Figure 7. EBSD of as-sprayed Ta coating diffused at 900 °C for 0.5 h: (a) image quality (IQ) map; (b) grain size map.

According to the above results, it seems that the interdiffusion rate of Ti–Ta at 900 °C (just above the phase transition temperature of Ti) is moderate, and the relatively small grains of Ta are beneficial to the strength of coating. Considering that the common temperature of about 800 °C~960 °C for the HIP of Ti and Ti alloys can achieve a good creep diffusion of particles and densification of materials [40–42], the reasonable temperature of 900 °C was selected as the HIP temperature for cold-sprayed Ti–Ta graded coatings subsequently in this study.

3.2. Microstructure of Ti–Ta Graded Coatings

Figure 8 illustrates the microstructural morphology of as-sprayed, unencapsulated and encapsulated HIPed Ti–Ta graded coatings. Compared to the distinct microscopic interface between Ti and Ta particles in the as-sprayed coating, obvious diffusion zones can be observed after HIP at 900 °C both with and without capsulation. Moreover, the macroscopic interface also transformed into metallurgical bonding by means of diffusion. The detailed microstructure of the interdiffusion zone is presented in Figure 9. The α -phase zone around Ti and the β -phase zone adjacent to Ta is separated by a layered distribution of the (α + β) biphasic zone, where the bright and light gray areas are β - and α -phase, respectively [19]. Unlike the Ti–Ta composite in reference [18,43,44], the HIPed Ti–Ta coatings in this study retained some pure Ti and Ta regions. Meanwhile, no significant Kirkendall voids could be found in the encapsulated HIPed samples. It could be expected that such characteristic can enhance the wave attenuation performance [6,7].

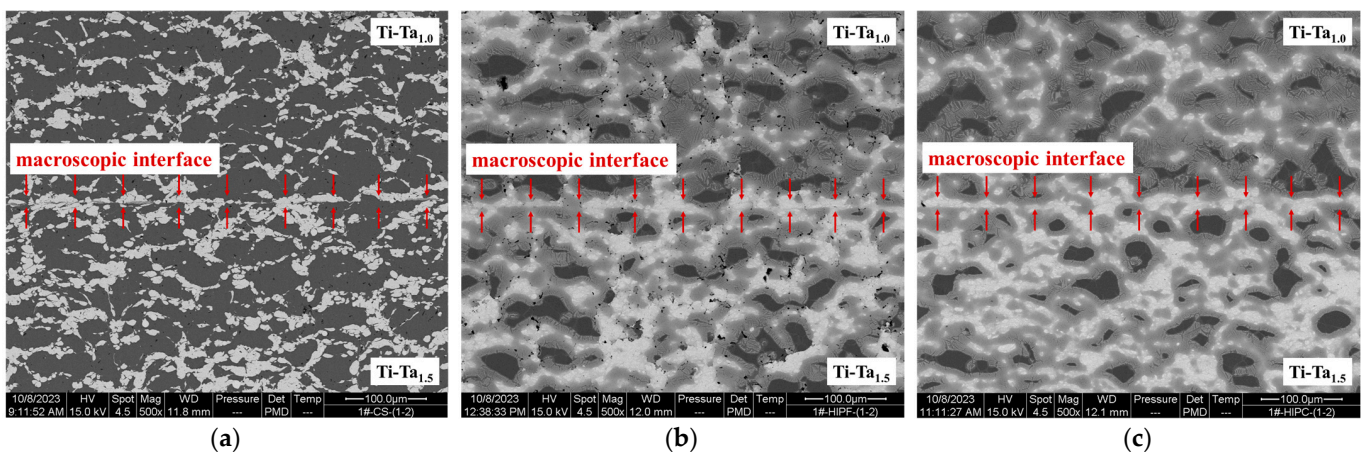


Figure 8. SEM of Ti–Ta graded materials: (a) as-sprayed; (b) unencapsulated; and (c) encapsulated HIP at 900 °C for 2 h.

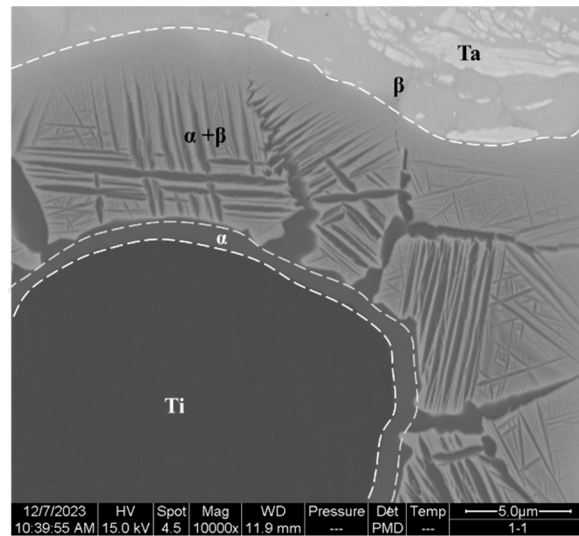


Figure 9. Typical microstructure morphology of encapsulated HIPed Ti–Ta coating.

Although the diffusion zones of unencapsulated and encapsulated HIP in Ti–Ta coating are similar, the porosity is quite different in the two cases. Some observable pores still exist in the unencapsulated HIPed coatings (Figure 8b), while the encapsulated HIPed coatings are dense (Figure 8c). For instance, Figure 10 presents the morphologies of the pores and the statistic porosity in the as-sprayed, unencapsulated and encapsulated HIP Ti–Ta_{1.5} coating. The pore size in the as-sprayed coating was 30–50 μm and the porosity was about 1.8%. After HIP, the porosity in the unencapsulated sample decreased to about 1% and the maximum pore size reduced to about 20 μm, whereas the encapsulated one was almost fully dense without any observable pores.

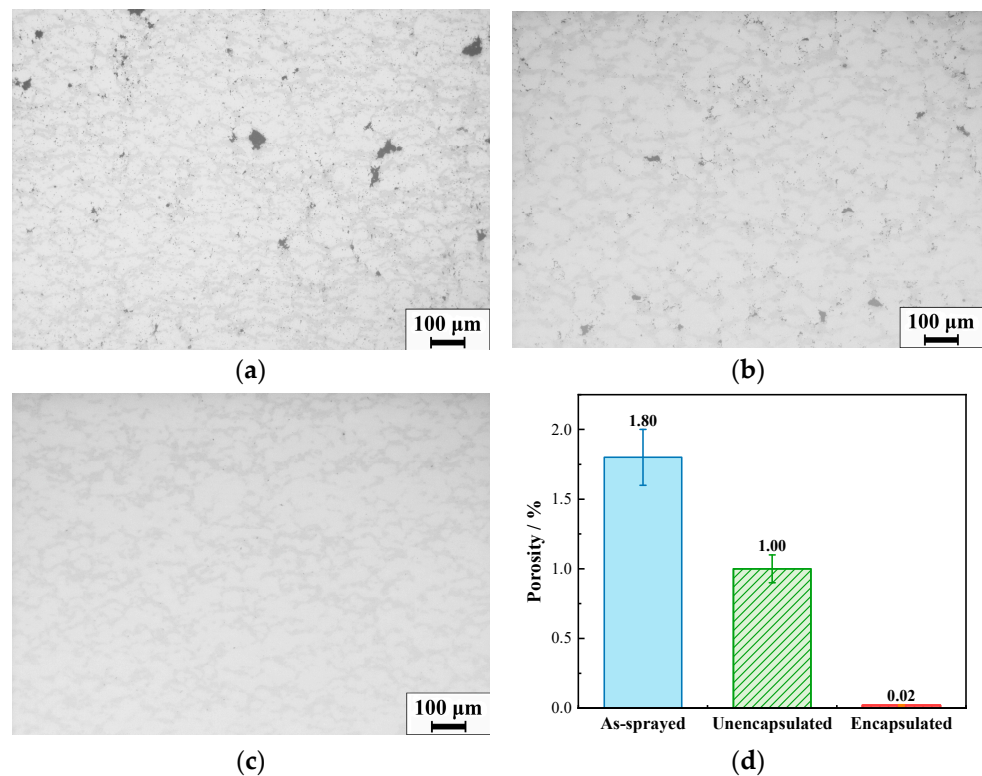


Figure 10. OM images of Ti–Ta_{1.5} coatings: (a) as-sprayed; (b) unencapsulated HIPed; (c) encapsulated HIPed; (d) porosity of different coatings.

This difference in the pores may involve the different densification mechanisms of unencapsulated and encapsulated HIP in cold-sprayed coatings. For laser additive manufactured materials, it has been proved that the internal closed pores can be effectively eliminated by unencapsulated HIP [25,26]. However, it was hard to eliminate the seemingly “closed pores” inside the coating by unencapsulated HIP in this study. This implies that the particle interface may act as the gas transfer channels for the working gas of HIP (Ar) and hinder the evolution of pore closure. In other words, these seemingly “closed pores” in the cold-sprayed coating were not actually closed.

As for encapsulated HIP, the capsule can hinder the entrance of external Ar and achieve densification effectively. Nevertheless, the densification mechanism may be different from that of LMAed material. Before HIP of LMAed, the Ar remaining in the closed pores is of large molecular size and low solubility. It was suggested that the argon pore can be pressed to tiny one ($<1\ \mu\text{m}$) with a pressure of $\sim 100\ \text{MPa}$, which is equal to the atmospheric pressure of HIP [45,46]. In this study, since the working gas of cold spray is N_2 , it is supposed that the pores in the as-sprayed coatings consist of N_2 . According to reference [47], N_2 can react with Ti under $800\ \text{C}\sim 1100\ \text{C}$ or dissolve in Ti. Therefore, the tiny pores cannot be just considered as residual pores full of compressed gas, although a similar size ($<1\ \mu\text{m}$) does remain in the encapsulated HIPed coatings. In contrast, under the HIP temperature of $900\ \text{C}$, the N_2 in Ti-Ta coatings may dissolve, react with Ti, or even diffuse through a specific channel to the surface of the coatings. To what extent these three modes contribute to the pore elimination in cold-sprayed Ti-Ta coatings needs to be further confirmed later.

3.3. Mechanical Properties of Ti-Ta Graded Coatings

Figure 11 shows the quasi-static tensile properties of as-sprayed and HIPed Ti-Ta coatings. The tensile strength and fracture strain of as-sprayed Ti-Ta_{1.5} are about 100 MPa and less than 1%, exhibiting a typical brittle fracture similar to that of the cold-sprayed pure Cu, Ti, stainless, and composite coatings [12–15]. After unencapsulated HIP, although the tensile strengths of Ti-Ta_{1.5} were improved significantly to about 389.5 MPa, the fracture strain (3.4%) was still far below that of the pure Ti or Ta. It is noteworthy that Ti-Ta_{1.5} exhibited excellent tensile properties after encapsulated HIP, with a tensile strength of 990.1 MPa, which is about eight times that of the as-sprayed sample. Meanwhile, the fracture strain also increased from less than 1% to 11.5%, which is similar to the pure Ti.

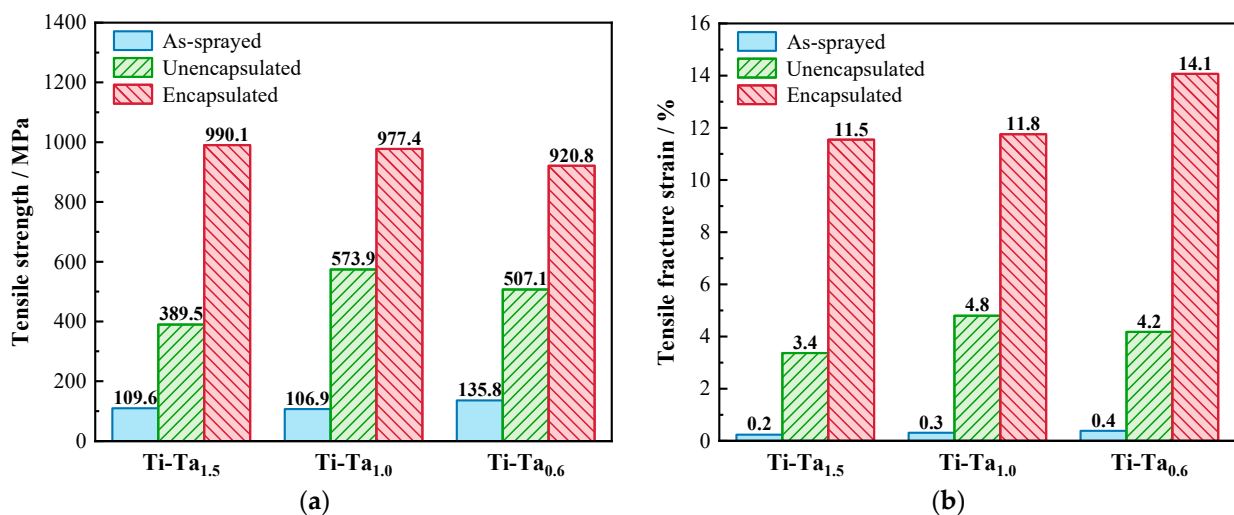


Figure 11. Tensile strength and fracture strain of as-sprayed and HIPed Ti-Ta coatings: (a) tensile strength; (b) fracture strain.

To understand the detailed fracture character, the fractured morphology of as-sprayed and HIPed Ti-Ta_{1.5} coatings is shown in Figure 12. For the as-sprayed coating, the debond-

ing of the particle interface can be observed clearly (Figure 12a). The fractured surface displays a dominant brittle morphology despite the fact that a few dimples can be found in the Ti–Ta diffusion zone for the unencapsulated HIPed sample. In the encapsulated HIPed coating, the fracture mode is dominated by ductile fracture, while the pure Ti region exhibits cleavage fracture. This can be attributed to the lack of effective slip planes in hcp structures (Figure 12c). Combined with the tensile test data, it can be determined that the elimination of micropores during encapsulated HIP was responsible for the dramatically improved tensile strength and plasticity.

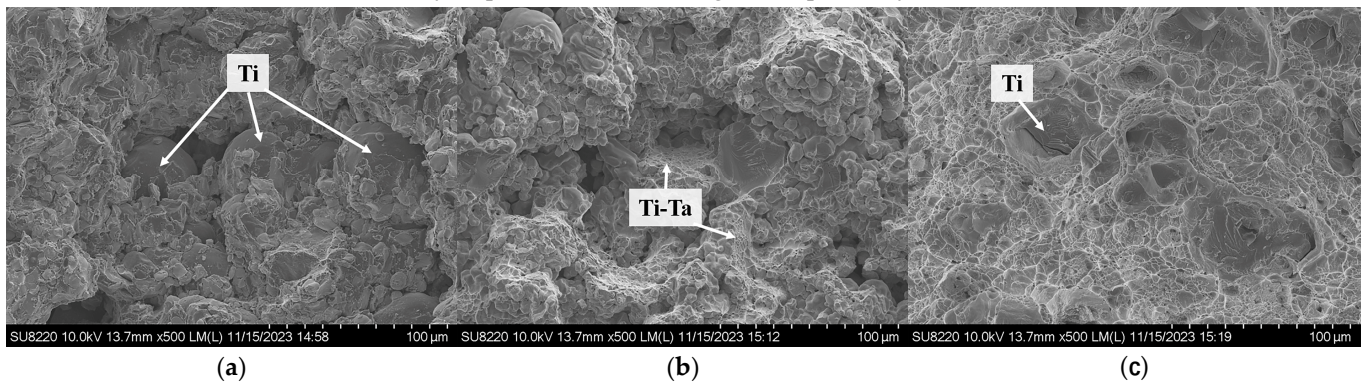


Figure 12. Quasi-static tensile fracture morphology of Ti–Ta_{1.5}: (a) as-sprayed; (b) unencapsulated HIPed; (c) encapsulated HIPed.

Another interesting phenomenon is that the tensile strength of the encapsulated HIPed Ti–Ta composite coatings was much higher than that of pure Ti and Ta. This strengthening relates to the diffusion region in the Ti–Ta coatings. Figure 13 shows the cross-sectional microstructures of the diffusion zone near the tensile fractured surface in the encapsulated HIPed Ti–Ta_{1.5} coating. It can be observed that the precipitate phases in the diffusion zone were bent under the tensile loading. The partially thin lath-like β -phases were completely cut off or formed obvious slip steps, while the thick, lath-like β -phases with acicular-like α -phases have less deformation and remain intact. Such a result indicates that the phase interface can hinder the slip of dislocations, while thick β -phases with fine acicular α precipitates are more effective [48,49]. In addition, solid-solution strengthening and fine-grain strengthening may also improve the strength to some extent [43,44].

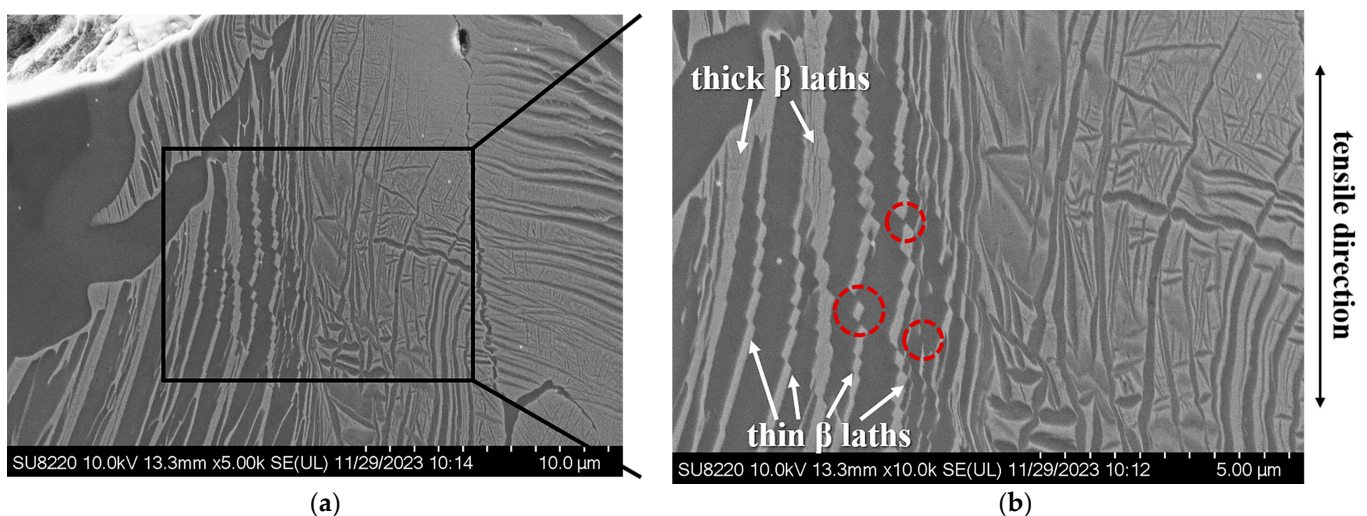


Figure 13. SEM of the tensile fracture cross-section of diffusion region in encapsulated HIPed Ti–Ta_{1.5} coating: (a) 5000 \times ; (b) 10,000 \times .

Although the deformation mechanism of the diffusion zone during the stretching process is similar to that of the Ti-Ta alloys in Wang’s research [48], the Ti-Ta coating in this study has better plasticity. This difference may be due to the coordinated deformation between remaining pure Ti or Ta parts in the Ti-Ta coatings. Some sub-cracks perpendicular to the stretching direction can be observed in pure Ti, as shown in Figure 14. In the ununiform stress field at microscale, the pure Ta has better plasticity and more easily coordinates deformation during tension. Consequently, the stress concentration in Ti may lead to the premature crack initiation.

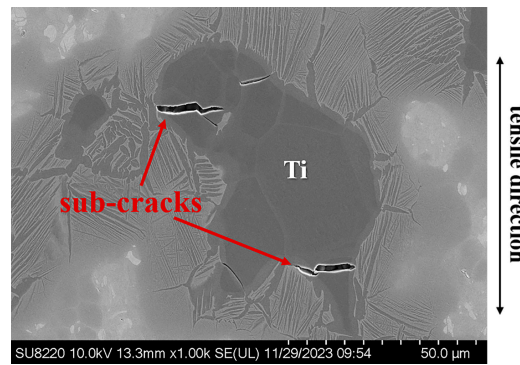


Figure 14. SEM of the tensile fracture cross-section of pure Ti in encapsulated HIPed Ti-Ta_{1.5} coating.

Regarding the graded structure, the macroscopic interfaces also play a role in the stability of the overall mechanical properties as well as the performance of each single layer. Therefore, the tensile property for the macroscopic interface is also of importance. Figure 15 shows the measured interfacial bonding strength of Ti-Ta_{1.5}/Ti-Ta_{1.0} and Ti-Ta_{1.0}/Ti-Ta_{0.6}, respectively. For the as-sprayed samples, the bonding strength (25 MPa) is far below the strength of single layer, and the fracture at the macroscopic interface is flat (Figure 15b). In HIPed samples, most of the fractured surfaces are located away from the macroscopic interfaces, and all the fracture surfaces are unsmooth (Figure 15c). This bonding strength is comparable to the strength of a single Ti-Ta layer, which can be attributed to the metallurgical bond in the macroscopic interface. Especially in the samples which were HIPed with capsules, the bonding strength (≥ 881 MPa) reached about twice that of the sample were HIPed without capsules. It can be inspected that the high bonding strength at the macroscopic interface is beneficial to prevent potential cracks under the tensile stress wave when it is used to attenuate the stress wave.

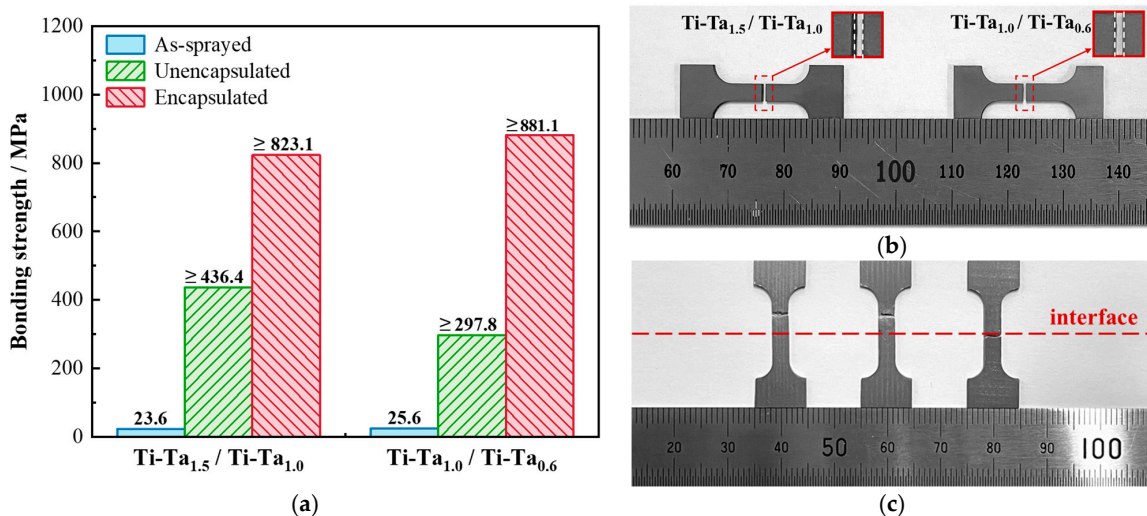


Figure 15. Bonding strength and fracture location of Ti-Ta graded coating: (a) bonding strength; fracture location in (b) as-sprayed and (c) HIPed graded coatings.

4. Conclusions

This work confirms that the special microstructure in cold-sprayed Ti–Ta couples significantly enhances the interdiffusion coefficient. The HIP temperature was selected as 900 °C, which controlled the Ti–Ta graded coating with limited diffusion successfully. The results shows that the encapsulated HIP can effectively reduce the porosity and pore size of the cold-sprayed Ti–Ta coatings. In the diffusion zone of Ti–Ta coatings, the phase interface can hinder the expansion of dislocations, which enhance the tensile strength to 990.1 MPa. Meanwhile, the pure Ta with good plasticity improved the plasticity of Ti–Ta coatings, resulting in a tensile fracture strain of 11.5%. In addition, the macroscopic interface in the cold-sprayed Ti–Ta graded coating forms a tight metallurgical bond after HIP, making the bonding strength comparable to that of each layer. It can be expected that the high bonding strength at the macroscopic interface is beneficial for mitigating the cracking risk when the graded coatings are subjected to the tensile stress wave.

Author Contributions: Conceptualization, X.N. and C.T.; methodology, Y.S.; validation, X.Y., C.F. and D.L.; formal analysis, Y.S.; investigation, Y.S.; writing—original draft preparation, Y.S.; writing—review and editing, X.N. All authors have read and agreed to the published version of the manuscript.

Funding: This research received no external funding.

Institutional Review Board Statement: Not applicable.

Informed Consent Statement: Not applicable.

Data Availability Statement: All data generated or analyzed during this study are included in this article.

Conflicts of Interest: Author D.L. and C.F. were employed by the company Chongqing Hongyu Precision Industry Group Co., Ltd. The remaining authors declare that the research was conducted in the absence of any commercial or financial relationships that could be construed as a potential conflict of interest.

References

1. Fernando, P.L.N.; Mohotti, D.; Remennikov, A.; Hazell, P.J.; Wang, H.; Amin, A. Experimental, numerical and analytical study on the shock wave propagation through impedance-graded multi-metallic systems. *Int. J. Mech. Sci.* **2020**, *178*, 105621. [[CrossRef](#)]
2. Hui, D.; Dutta, P.K. A new concept of shock mitigation by impedance-graded materials. *Compos. Part B* **2011**, *42*, 2181–2184. [[CrossRef](#)]
3. Tasdemirci, A.; Hall, I.W. The effects of plastic deformation on stress wave propagation in multi-layer materials. *Int. J. Impact. Eng.* **2007**, *34*, 1797–1813. [[CrossRef](#)]
4. Fernando, P.L.N.; Mohotti, D.; Remennikov, A. Behaviour of explosively welded impedance-graded multi-metal composite plates under near-field blast loads. *Int. J. Mech. Sci.* **2019**, *163*, 105124. [[CrossRef](#)]
5. Fernando, P.L.N.; Mohotti, D.; Remennikov, A.; Hazell, P.J.; Wang, H.; Amin, A. Stress propagation and debonding effects in impedance-graded multi-metallic systems under impact loading. *Int. J. Prot. Struct.* **2021**, *12*, 3–21. [[CrossRef](#)]
6. Zou, G.; Liang, Z.; Na, X.; Wang, X.; Chang, Z.; Yang, Y.; Zhao, P. Study of stress wave attenuation characteristics of particle ceramic embedded polyurethane composites. *Mater. Today Commun.* **2023**, *37*, 107057. [[CrossRef](#)]
7. Yu, Y.; Li, H.; Hu, X.; Geng, K.; Zhang, Q.; Peng, W.; Yuan, Y.; Zhang, Z.; Wang, B. Fast stress wave attenuation in bioinspired composites with distributed soft particles modulating hard matrices. *EML* **2023**, *61*, 102021. [[CrossRef](#)]
8. Boruah, D.; Zhang, X.; Doré, M.J. An Analytical Method for Predicting Residual Stress Distribution in Selective Laser Melted/Sintered Alloys. In Proceedings of the 10th European Conference on Residual Stresses (ECRS-10), Leuven, Belgium, 11–14 September 2018.
9. Shiomi, M.; Osakada, K.; Nakamura, K.; Yamashita, T.; Abe, F. Residual Stress within Metallic Model Made by Selective Laser Melting Process. *CIRP Ann.* **2004**, *53*, 195–198. [[CrossRef](#)]
10. Lucio, M.D.S.; Kultayeva, S.; Kim, Y.-W. Improved mechanical strength and thermal resistance of porous SiC ceramics with gradient pore sizes. *J. Eur. Ceram. Soc.* **2022**, *42*, 6785–6794. [[CrossRef](#)]
11. Huang, C.; List, A.; Wiehler, L.; Schulze, M.; Gärtner, F.; Klassen, T. Cold spray deposition of graded Al-SiC composites. *Addit. Manuf.* **2022**, *59*, 103116. [[CrossRef](#)]
12. Judas, J.; Zapletal, J.; Řehořek, L.; Jan, V. Effects of annealing temperature on microstructure and mechanical properties of cold sprayed AA7075. *Procedia Struct. Integr.* **2023**, *43*, 160–165. [[CrossRef](#)]
13. Xie, X.; Chen, C.; Chen, Z.; Addad, A.; Xie, Y.; Wu, H.; Verdy, C.; Wang, Y.; Wang, J.; Ren, Z.; et al. Effect of annealing treatment on microstructure and mechanical properties of cold sprayed TiB₂/AlSi10Mg composites. *Surf. Interfaces* **2021**, *26*, 101341. [[CrossRef](#)]

14. Huang, R.; Sone, M.; Ma, W.; Fukanuma, H. The effects of heat treatment on the mechanical properties of cold-sprayed coatings. *Surf. Coat. Technol.* **2015**, *261*, 278–288. [[CrossRef](#)]
15. Huang, C.; Arseenko, M.; Zhao, L.; Xie, Y.; Elsenberg, A.; Li, W.; Gärtner, F.; Simar, A.; Klassen, T. Property prediction and crack growth behavior in cold sprayed Cu deposits. *Mater. Des.* **2021**, *206*, 109826. [[CrossRef](#)]
16. Wu, D.; Li, W.; Liu, K.; Yang, Y.; Hao, S. Optimization of cold spray additive manufactured AA2024/Al₂O₃ metal matrix composite with heat treatment. *JMST* **2022**, *106*, 211–224. [[CrossRef](#)]
17. Han, P.; Lin, J.; Wang, W.; Liu, Z.; Xiang, Y.; Zhang, T.; Liu, Q.; Guan, X.; Qiao, K.; Xie, Y.; et al. Friction Stir Processing of Cold-Sprayed High-Entropy Alloy Particles Reinforced Aluminum Matrix Composites: Corrosion and Wear Properties. *Met. Mater. Int.* **2023**, *29*, 845–860. [[CrossRef](#)]
18. Xu, S.; Qiu, J.; Zhang, H.; Liu, Y. Evolution of nano-scaled lamellae and its effect on strength of Ti–Ta composite. *Mater. Sci. Eng. A* **2021**, *805*, 140552. [[CrossRef](#)]
19. Tang, J.; Tariq, N.U.H.; Zhao, Z.; Guo, M.; Liu, H.; Ren, Y.; Cui, X.; Shen, Y.; Wang, J.; Xiong, T. Microstructure and Mechanical Properties of Ti–Ta Composites Prepared Through Cold Spray Additive Manufacturing. *Acta Metall. Sin. Engl. Lett.* **2022**, *35*, 1465–1476. [[CrossRef](#)]
20. Askill, J. Environmental Effects on the Diffusion of Ta¹⁸² in B.C.C. Titanium. *Phys. Status. Solidi. (B)* **1966**, *16*, K63–K65. [[CrossRef](#)]
21. Ansel, D.; Thibon, I.; Boliveau, M.; Debuigne, J. Interdiffusion in the body cubic centered β -phase of Ta–Ti alloys. *Acta Mater.* **1998**, *46*, 423–430. [[CrossRef](#)]
22. Wang, K.; Liu, X.; Liu, T.; He, C.; Liu, J. Investigation on diffusion kinetics of Ti-X binary systems at 1300–1500 °C. *J. Mater. Res. Technol.* **2023**, *25*, 1684–1695. [[CrossRef](#)]
23. Tang, J.; Zhao, Z.; Li, N.; Qiu, X.; Shen, Y.; Cui, X.; Du, H.; Wang, J.; Xiong, T. Influence of feedstock powder on microstructure and mechanical properties of Ta cold spray depositions. *Surf. Coat. Technol.* **2019**, *377*, 124903. [[CrossRef](#)]
24. Yin, S.; Cizek, J.; Cupera, J.; Hassani, M.; Luo, X.; Jenkins, R.; Xie, Y.; Li, W.; Lupoi, R. Formation conditions of vortex-like intermixing interfaces in cold spray. *Mater. Des.* **2021**, *200*, 109444. [[CrossRef](#)]
25. Tammam-Williams, S.; Withers, P.J.; Todd, I.; Prangnell, P.B. The Effectiveness of Hot Isostatic Pressing for Closing Porosity in Titanium Parts Manufactured by Selective Electron Beam Melting. *Metall. Mater. Trans. A* **2016**, *47A*, 1939–1946. [[CrossRef](#)]
26. du Plessis, A.; Macdonald, E. Hot isostatic pressing in metal additive manufacturing: X-ray tomography reveals details of pore closure. *Addit. Manuf.* **2020**, *34*, 101191. [[CrossRef](#)]
27. Blose, R.E.; Walker, B.H.; Walker, R.M.; Froes, S.H. New opportunities to use cold spray process for applying additive features to titanium alloys. *MPR* **2006**, *61*, 30–37. [[CrossRef](#)]
28. Blose, R.E. Spray forming titanium alloys using the cold spray process. In Proceedings of the International Thermal Spray Conference (ITSC 2005), Basel, Switzerland, 2–4 May 2005.
29. Petrovskiy, P.; Travyanov, A.; Cheverikin, V.V.; Cheresheva, A.A.; Sova, A.; Smurov, I. Effect of encapsulated hot isostatic pressing on properties of Ti6Al4V deposits produced by cold spray. *Int. J. Adv. Manuf. Technol.* **2020**, *107*, 437–449. [[CrossRef](#)]
30. Chen, C.; Xie, Y.; Yan, X.; Yin, S.; Fukanuma, H.; Huang, R.; Zhao, R.; Wang, J.; Ren, Z.; Liu, M.; et al. Effect of hot isostatic pressing (HIP) on microstructure and mechanical properties of Ti6Al4V alloy fabricated by cold spray additive manufacturing. *Addit. Manuf.* **2019**, *27*, 595–605. [[CrossRef](#)]
31. Petrovskiy, P.; Khomutov, M.; Cheverikin, V.; Travyanov, A.; Sova, A.; Smurov, I. Influence of hot isostatic pressing on the properties of 316L stainless steel, Al-Mg-Sc-Zr alloy, titanium and Ti6Al4V cold spray deposits. *Surf. Coat. Technol.* **2021**, *405*, 126736. [[CrossRef](#)]
32. Petrovskiy, P.; Sova, A.; Doubenskaia, M.; Smurov, I. Influence of hot isostatic pressing on structure and properties of titanium cold-spray deposits. *Int. J. Adv. Manuf. Technol.* **2019**, *102*, 819–827. [[CrossRef](#)]
33. Mehrer, H. *Diffusion in Solids: Fundamentals, Methods, Materials, Diffusion-Controlled Processes*; Springer: Berlin/Heidelberg, Germany, 2007.
34. Murray, J.L. The Ta-Ti (Tantalum-Titanium) system. *Bull. Alloy Phase Diagr.* **1981**, *2*, 62–66. [[CrossRef](#)]
35. Reiser, J.; Franke, P.; Weingärtner, T.; Hoffmann, J.; Hoffmann, A.; Rieth, M. Tungsten laminates made of ultrafine-grained (UFG) tungsten foil–Ageing of tungsten–titanium (W–Ti) laminates. *Int. J. Refract. Met. Hard Mater.* **2015**, *51*, 264–274. [[CrossRef](#)]
36. Wang, S.; Xie, M.Y.; Huang, H.B.; Kang, M.; Liu, R.; Chen, C.; Zhang, Z.; Zhong, Z.H.; Wu, Y.C. Diffusion behavior and bending fracture mechanism of W/Ti multilayer composites. *J. Alloys Compd.* **2021**, *879*, 160451. [[CrossRef](#)]
37. Yin, S.; Fan, N.; Huang, C.; Xie, Y.; Zhang, C.; Lupoi, R.; Li, W. Towards high-strength cold spray additive manufactured metals: Methods, mechanisms, and properties. *JMST* **2024**, *170*, 47–64. [[CrossRef](#)]
38. Zou, Y.; Qin, W.; Irissou, E.; Legoux, J.-G.; Yue, S.; Szpunar, J.A. Dynamic recrystallization in the particle/particle interfacial region of cold-sprayed nickel coating: Electron backscatter diffraction characterization. *Scr. Mater.* **2009**, *61*, 899–902. [[CrossRef](#)]
39. William, D.C., Jr. *Fundamentals of Materials Science and Engineering*; Anderson, W., Ed.; John Wiley & Sons: New York, NY, USA, 2001.
40. Bocanegra-Bernal, M.H. Hot Isostatic Pressing (HIP) technology and its applications to metals and ceramics. *J. Mater. Sci.* **2004**, *39*, 6399–6420. [[CrossRef](#)]
41. Xiao, Y.; Lang, L.-H.; Xu, W.-C.; Zhang, D.-X. Diffusion bonding of Ti–6Al–4V titanium alloy powder and solid by hot isostatic pressing. *Trans. Nonferrous Met. Soc. China* **2022**, *32*, 3587–3595. [[CrossRef](#)]
42. Atkinson, H.V.; Davies, S. Fundamental aspects of hot isostatic pressing: An overview. *Metall. Mater. Trans. A* **2000**, *31*, 2981–3000. [[CrossRef](#)]

43. Xu, S.; Du, M.; Li, J.; Yan, K.; Cai, B.; He, Q.; Fang, Q.; Magdysyuk, O.; Liu, B.; Yang, Y.; et al. Bio-mimic Ti–Ta composite with hierarchical “Brick-and-Mortar” microstructure. *Materialia* **2019**, *8*, 100463. [[CrossRef](#)]
44. Xu, S.; Liu, Y.; Yang, C.; Zhao, H.; Liu, B.; Li, J.; Song, M. Compositionally gradient Ti–Ta metal-metal composite with ultra-high strength. *Mater. Sci. Eng. A* **2018**, *712*, 386–393. [[CrossRef](#)]
45. Tammam-Williams, S.; Withers, P.J.; Todd, I.; Prangnell, P.B. Porosity regrowth during heat treatment of hot isostatically pressed additively manufactured titanium components. *Scr. Mater.* **2016**, *122*, 72–76. [[CrossRef](#)]
46. Shao, S.; Mahtabi, M.J.; Shamsaei, N.; Thompson, S.M. Solubility of argon in laser additive manufactured α -titanium under hot isostatic pressing condition. *Comput. Mater. Sci.* **2017**, *131*, 209–219. [[CrossRef](#)]
47. Mohammadi, M.; Akbari, A.; Warchomicka, F.; Pichon, L. Depth profiling characterization of the nitride layers on gas nitrided commercially pure titanium. *Mater. Charact.* **2021**, *181*, 111453. [[CrossRef](#)]
48. Wang, C.; Cai, Q.; Liu, J.; Yan, X. Strengthening mechanism of lamellar-structured Ti–Ta alloys prepared by powder metallurgy. *J. Mater. Res. Technol.* **2022**, *21*, 2868–2879. [[CrossRef](#)]
49. Sadeghpour, S.; Abbasi, S.M.; Morakabati, M.; Bruschi, S. Correlation between alpha phase morphology and tensile properties of a new beta titanium alloy. *Mater. Des.* **2017**, *121*, 24–35. [[CrossRef](#)]

Disclaimer/Publisher’s Note: The statements, opinions and data contained in all publications are solely those of the individual author(s) and contributor(s) and not of MDPI and/or the editor(s). MDPI and/or the editor(s) disclaim responsibility for any injury to people or property resulting from any ideas, methods, instructions or products referred to in the content.